

ARTICLE OPEN



Laser-clad Inconel 625 coatings on Q245R structure steel: microstructure, wear and corrosion resistance

Wanyuan Gui¹, Cheng Zhong¹, Junyi Gu¹, Yuhang Ding¹, Xiaoming Wang¹, Tao Wu¹, Yongfeng Liang², Jingyan Qin³, Yuhai Qu⁴ and Junpin Lin²

In this work, ultra-low dilution rate Inconel 625 coatings with a thickness of ~534.4 μm were prepared by high-speed laser cladding technique on the Q245R steel. The XRD and TEM results show that the Inconel 625 coatings are mainly composed of the Nb and Mo-enriched laves phase with hexagonal close-packed (HCP) structure and the γ-Ni phase with face-centered-cubic (FCC) structure. The cellular crystal, column crystal, and equiaxed dendritic crystal were observed in the bottom, middle, and top of the Inconel 625 coatings from SEM results, respectively. The wear resistance and corrosion resistance of Q245R steel are significantly improved by high-speed laser cladding Inconel 625 coatings. In addition, the low dilution rate is beneficial for improving the wear and corrosion resistance of high-speed laser cladding Inconel 625 coatings. These findings may provide a method to design the wear and corrosion resistance of coatings on steel's surface.

npj Materials Degradation (2022)6:37; <https://doi.org/10.1038/s41529-022-00247-z>

INTRODUCTION

Q245R structural steel, known as engineering metallic structural materials, is currently widely applied in the boilers and pressure vessel industry due to its unique properties, such as excellent plasticity, toughness, and welding performance¹. The surface of boilers and pressure vessels or the area near the surface may be damaged by wear, corrosion, and fatigue during long-term service. The sustained damage will result in severe damage to the surface of the Q245R structural steel until it can not be used anymore². Therefore, it is urgent to improve the wear resistance and corrosion resistance of the Q245R structural steel surface.

There are two main approaches to enhance wear resistance and corrosion resistance of metals substrate surface: alloy design and surface coating^{3–6}. Past research indicates that the improvement in the wear and corrosion resistance of substrate surface relies on surface coating rather than alloy design^{4,5}. Several surface modification techniques had been carried out to fabricate protective coatings on the substrate surface, such as electroplating⁷, diffusion treatment⁸, thermal spray⁹, cold spray¹⁰, surfacing¹¹, and laser cladding technology^{12–15}. Among numerous surface modification techniques, laser cladding is the most promising surface modification technique due to the fact that it produces high-quality, compactness, and crack-free coatings along with remarkable physical and chemical performance^{16–19}. However, traditional laser cladding is limited by powder feeding mode and low cladding speed. The physical and chemical performances of coating fabricated by traditional laser cladding technique always degrade severely since an extensive amount of heat input introduces amount additional elements in the substrate into the cladding coating. In addition, most of the laser energy is absorbed by the substrate because of the low cladding speed, making thin components seriously deformed¹². Compared with the conventional laser cladding technique, the high-speed laser cladding technique exhibits better coupling of a laser beam and powder flow via redesigning the coaxial powder feeding

nozzle^{20,21} and thus the powder particles could be heated to the melting point before guiding into the molten pool. Owing to the limited transmitted laser energy, a micro-molten pool could be formed on the substrate so that the coating with a low dilution ratio and metallurgical bonding could be produced and an excellent combination of physical performance and chemical performance could be achieved in the coating prepared by high-speed laser cladding technique.

Fabricating Inconel 625 coating on Q245R steel has great potential for enhancing the surface wear resistance and corrosion resistance of Q245R steel since the Inconel 625 has outstanding mechanical properties and excellent corrosion resistance^{22–24}. Here, a high-speed laser deposition technique was used to successfully deposit Inconel 625 coatings on Q245R steel with a dilution rate of less than 2.6% at a cladding speed of 5 m/min. The phase formation and microstructure evolution of the cladding were characterized by X-ray diffraction, field emission scanning electron microscopy, electron backscattered diffraction, and transmission electron microscopy. The wear resistance and hardness were measured by friction and wear instrument and microhardness tester. The polarization curves were tested by an electrochemical workstation. The effects of dilution rate on wear resistance and corrosion resistance were also presented.

RESULTS AND DISCUSSIONS

Phase structure and microstructural characteristics

To identify the phase composition of Q245R steel plate substrate and Inconel 625 coating, XRD measurements were performed. Figure 1 shows the XRD patterns of the Q245R steel substrate and the Inconel 625 coating. Apparently, the diffraction pattern of the Q245 steel substrate can be indexed as the α-Fe phase. Careful indexations of the pattern of Inconel 625 coating indicate that the coating mainly consists of the γ-Ni phase^{25–27}.

¹National Center for Materials Service Safety, University of Science and Technology Beijing, Beijing 100083, China. ²State Key Laboratory for Advanced Metals and Materials, University of Science and Technology Beijing, Beijing 100083, China. ³School of Mechanical Engineering, University of Science and Technology Beijing, Beijing 100083, China. ⁴School of Materials Science and Engineering, Nanchang University, Nanchang 330031, China. ✉email: yhqu@ncu.edu.cn; linjunpin@ustb.edu.cn

The formation of solidification microstructure in laser-based additive manufacturing (AM) techniques is readily described by following Eq. (1)²⁸:

$$\frac{G}{R} < \frac{m\omega}{D} \frac{1 - k_0}{k_0} \quad (1)$$

Where G , R , ΔT , W_0 , K_0 , and D represent temperature gradient, solidification growth rate, undercooling, the initial composition of a component, average solute distribution coefficient of the component, and liquid diffusivity, respectively. The effects of G and R on the developed microstructures are summarized as follows: the high growth rate results in a low-to-moderate G/R ratio and pushes the microstructure towards a planar or cellular structure in a single layer of AM fabricated specimens. While

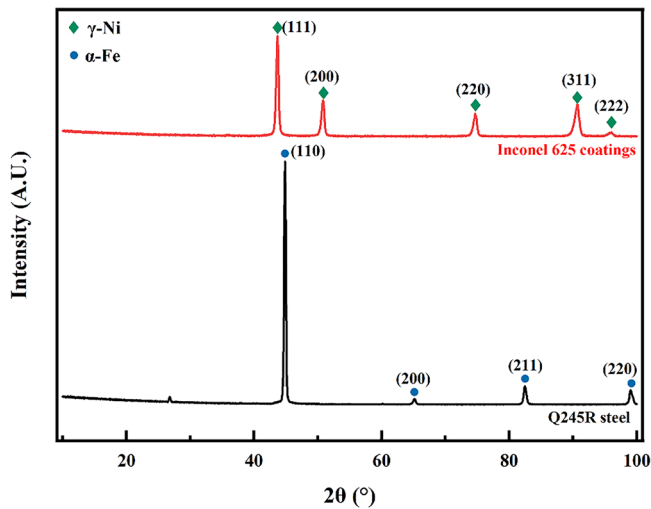


Fig. 1 X-ray diffraction patterns of Q245 steel substrate (black) and Inconel 625 coatings on Q245R steel (red).

columnar and equiaxed dendrites are commonly observed in multi-layer AM fabricated specimens^{28,29}.

Figure 2 displays the secondary electron images of the laser-clad specimen. From Fig. 2a, it can be found that the Inconel 625 coatings with a thickness of about 534.4 μm exhibit a uniform dense structure with small amounts of particulate matter distributed on the surface of the Inconel 625 coatings. The high growth rate results in a low-to-moderate G/R ratio and pushes the microstructure towards a cellular structure that appears at the bottom of the coating, as shown in Fig. 2b. From Fig. 2c and 2d, it can be found that the columnar and the equiaxed dendrites appear in the middle and top of the coating, respectively. Compared to the bottom part of the coating, the rest parts of the coating have a higher solidification rate (R) and moderate temperature gradients due to the fact that the Inconel 625 coatings experience a repetitious remelt (overlapping: 80%). Thus, the columnar dendrites are observed in the middle zone of the coating. There are two reasons for promoting the formation of equiaxed dendrites at the top of the coating. On the one hand, the top zone of the coating was exposed to the air and thus the big cooling rate (undercooling) of the top zone, which promotes the formation of equiaxed dendrites. On the other hand, local microsegregation lowers the melting point and may increase the likelihood of additional nucleation ahead of the dendritic front and inhibits the growth of columnar crystals^{28,29}.

The grain morphology, grain boundary, grain distribution, and grain boundary misorientation of Inconel 625 coatings were also characterized by EBSD and the results are displayed in Fig. 3. From the inverse pole figure of Inconel 625 coatings (Fig. 3a), most of the grains show a relatively scattered with no preferred orientation. The results also show that the internal orientations inside individual grains are uniform, suggesting the absence of any orientation gradient. Figure 3b is the corresponding EBSD band contrast map in which the grain boundaries can be distinguished by color (green line: angle 2°–15°, red line: angle 5–15°, black line: angle >15°). The results show that most grain boundaries of the γ -phase have high misorientation angles,

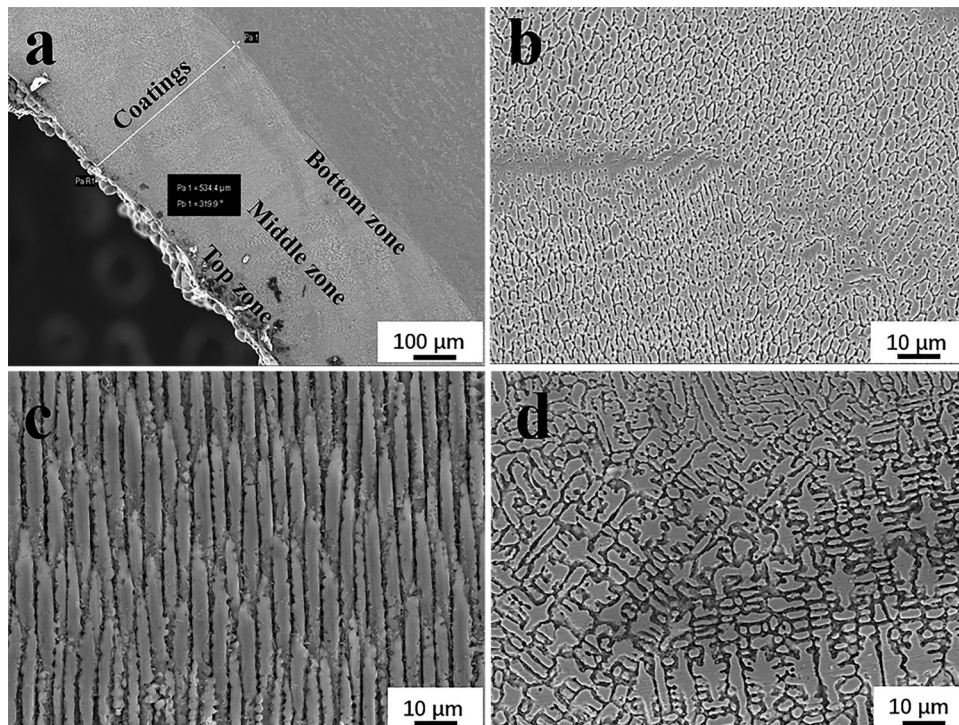


Fig. 2 FESEM images of Inconel 625 coatings on Q245R steel. **a** Cross-sectional; **b** bottom zone; **c** middle zone; **d** top zone.

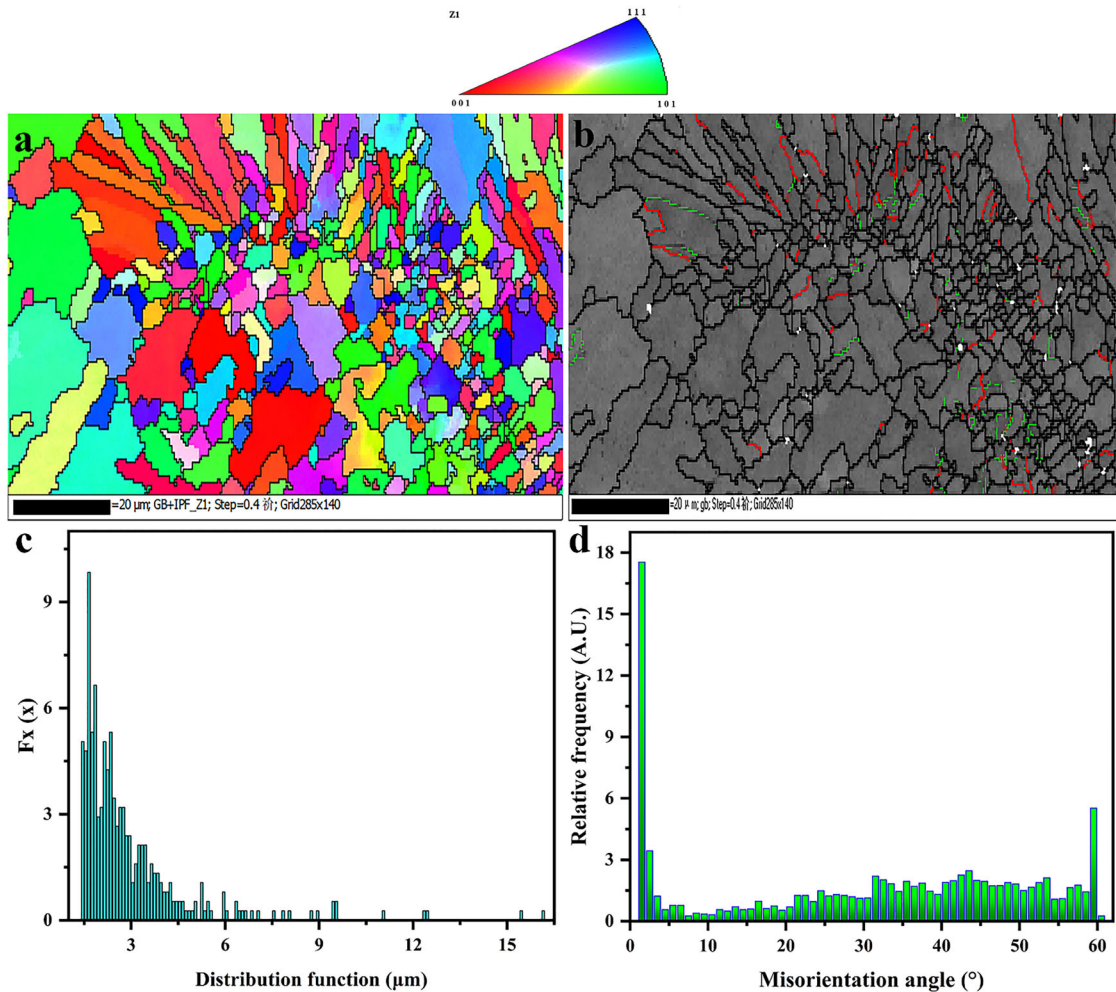


Fig. 3 EBSD analysis for Inconel 625 coatings on Q245R steel (S6). **a** Inverse pole figure; **b** boundaries distribution; **c** grain distribution corresponding to (a); **d** grain boundary misorientation corresponding to (a).

indicating that there are few residual stresses accumulated in the Inconel 625 coatings. The reason for the formation of stray grain is attributed to be related to the constitutive supercooling^{30,31}, where the segregation of the solute atoms ahead of the solidification front modifies the solidification temperature of the alloy to increase the degree of undercooling without physical changes in the temperature or the temperature gradient. Most of the grain distribution was estimated to be $<5\ \mu\text{m}$ from the grain distribution function figure (Fig. 3c). Figure 3d shows the columnar statistical distribution of grain misorientation of the specimen. 71.46% of the grain boundaries are high angle grain boundaries ($>15^\circ$), while the rest (28.54%) grain boundaries are low angle grain boundaries ($<15^\circ$). It is worth noting that the grain boundaries located around $2\text{--}5^\circ$ account for 22.82%. The grain boundaries located around $2\text{--}5^\circ$ are commonly considered sub-grain boundaries, which are caused by dislocation rearrangement^{32,33}. The large proportion of sub-grain boundaries indicates that the dislocation rearrangement is serious during the SLM process. The same result can also be found in the TEM study.

Further phase identification for Inconel 625 coating was carried out by using TEM and the results are shown in Fig. 4. Figure 4a shows the bright field image for an area with coexisting phases. Figure 4b, and 4c display the selected area diffraction patterns for phase A and phase B in Fig. 4a, respectively. As shown in Fig. 4b and 4c, the phases A and B shows the characteristics of the γ -Ni phase with FCC structure and laves

phase with HCP structure. The chemical composition of the laves phase (phase B) was analyzed by EDS and the results are listed in Table 1. From Table 1, it can be found that the laves phase is rich in Nb and Mo. Figure 4d shows the bright field image for an area with the interface between Inconel 625 coatings and Q245R steel substrate. Figure 4e, and 4f display the selected area diffraction patterns for phase C and phase D in Fig. 4d, respectively. As shown in Fig. 4e and 4f, the phases C and D show the characteristics of the α -Fe phase with BCC structure and γ -Ni phase with FCC structure. Therefore, the top zone and the bottom zone in Fig. 4d are the Q245R steel substrate and the Inconel 625 coating. These results from TEM observations are in agreement with the XRD results (Fig. 1). In addition, as shown in Fig. 4d, dislocation tangles can be observed. The occurrence of dislocation structures can be ascribed to the residual stress of the coating formed during the high-speed laser cladding process, which is consistent with the EBSD analysis.

Figure 5 shows the variations trends in average roughness of the Inconel 625 coating surface (the S6 sample). There is a clear ravine-like texture existing on the surface of the Inconel 625 coating. There is a big height fluctuation (about $67.044\text{--}108.707\ \mu\text{m}$) in the microscopic texture, which indicates the Q245R steel substrate began to form the rough portions during the high-speed laser cladding process. And the average roughness value (Ra) of Inconel 625 coating was about $20\ \mu\text{m}$.

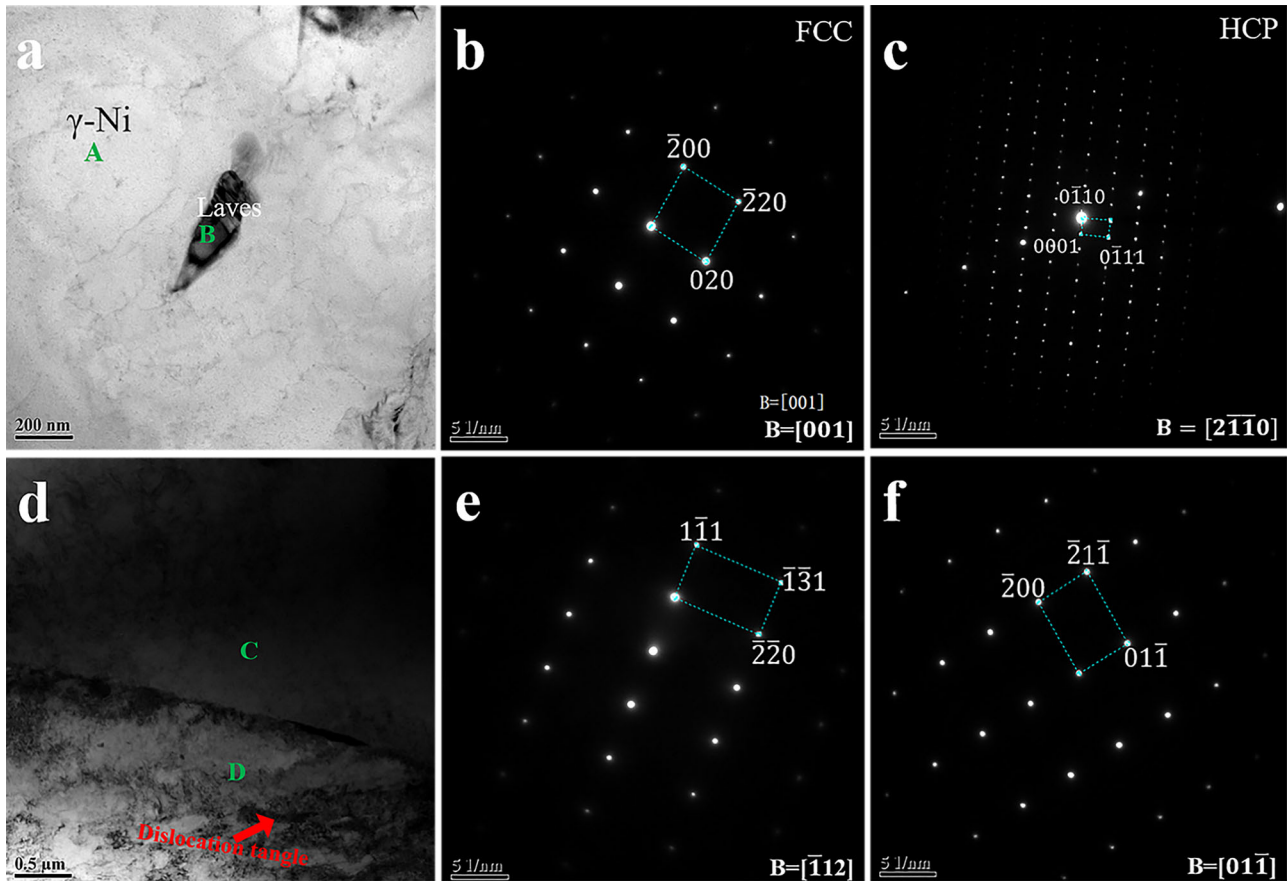


Fig. 4 TEM image of Inconel 625 coatings on Q245R steel (S6). **a** Top view; **b**, **c** selected area diffraction patterns for phase A and B corresponding to **a**; **d** bottom to top views; **e**, **f** selected area diffraction patterns for phase C and D corresponding to **(d)**.

Element	Weight %	Atomic %	Correction	Uncert. %	k-Factor
N	4.85	24.24	0.16	0.28	3.536
Cr	5.19	6.98	0.09	0.99	1.268
Ni	2.63	3.14	0.07	0.99	1.453
Nb	81.57	61.43	0.64	0.99	3.714
Mo	5.74	4.18	0.17	0.98	4.047

Dilution rate

Dilution rate is an important factor affecting the properties of laser cladding³⁴. An accurate estimate of dilution rate in direct laser fabrication is important in order to improve the surface quality and obtain the excellent properties of the cladding layer. There are two common methods for calculating dilution rate: one is through the geometry of the molten pool, and the other is through changing the composition of coating^{35,36}. Due to the geometry of the molten pool being seriously damaged after multi-pass laser cladding with a high overlap rate (80%), calculating the dilution rate through the geometry of molten pool is not applicable anymore. Here, the dilution rate was evaluated through the composition of coating variation, and the dilution rate (η) of coatings were calculated according to the equation below³⁶:

$$\eta = \frac{\rho_c(X_{c+s} - X_c)}{\rho_s(X_s - X_{c+s}) + \rho_c(X_{c+s} - X_c)} \quad (2)$$

Where ρ_s and ρ_c represent the density of Q245R steel substrate and Inconel 625 coatings respectively. And X_s , X_{cr} and X_{c+s} represent the mass fraction of Fe element in Q245R steel

substrate, Inconel 625 powder, and Inconel 625 coatings, respectively. A number of studies have been undertaken in this work to explore the relationship between the laser power, powder feeding rate, cladding speed, and the dilution rate of the coatings. Our results indicated that powder feeding rate was the main influential factor, cladding speed was next, and finally, the laser power.

Compared with conventional laser cladding coating (with 1–2 mm thickness, and dilution rate >15%)³⁷, the high-speed laser cladding coating has a smaller thickness (416–715 μm) and lower dilution rate (0.28–2.6%), as shown in Table 2. Ultra-low dilution rate Inconel 625 coatings (S6: 0.28) was prepared by using the optimal parameters: laser power of 1520 W, powder feeding rate of 22.1 g/min, and cladding speed of 3 m/min. The lower dilution rate is mean that only a very thin layer of the substrate has to be melted in order to achieve metallurgical bonding with coatings, as well as maintain the original properties of the coatings materials.

Microhardness and wear resistance

Figure 6a shows the microhardness of the Inconel 625 coatings on Q245R steel fabricated by high-speed laser cladding with different dilution rates. Apparently, the microhardness of all specimens (S4, S5, and S6) increases at the beginning and then tends to be stable. These results suggest that the hardness of the coating (350 $\text{HV}_{0.1}$) is larger than that of the interface between coating and substrate and the hardness of the interface is higher than that of the substrate (150 $\text{HV}_{0.1}$). In addition, it can be found that the dilution rate has a significant influence on the hardness of the interface in the specimens but has little influence on the hardness of the

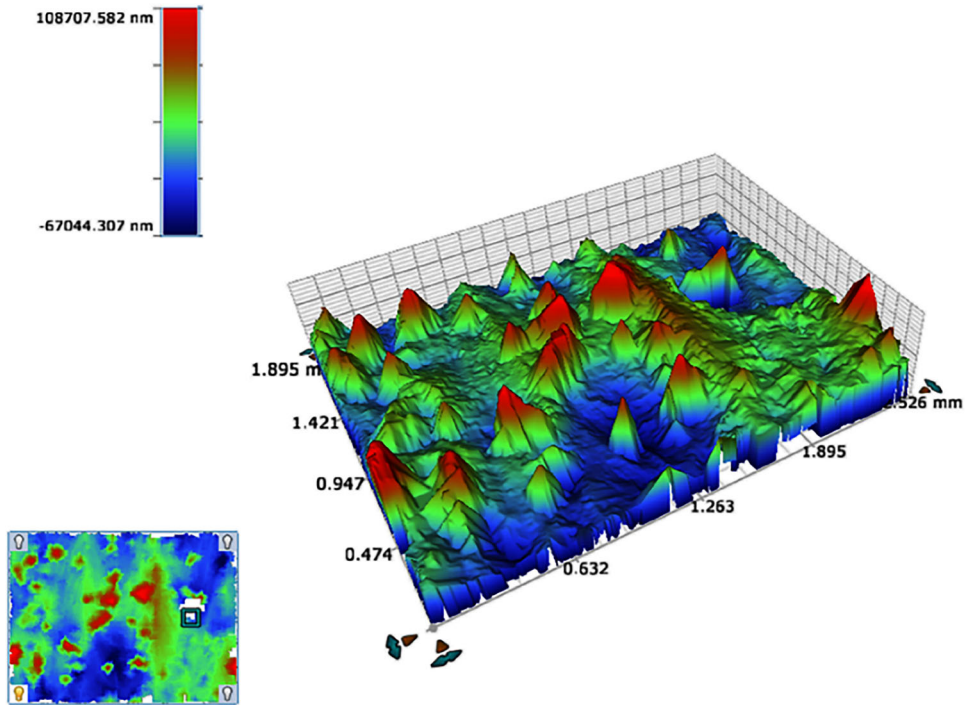


Fig. 5 3D topography of Inconel 625 coatings on Q245R steel substrate (S6).

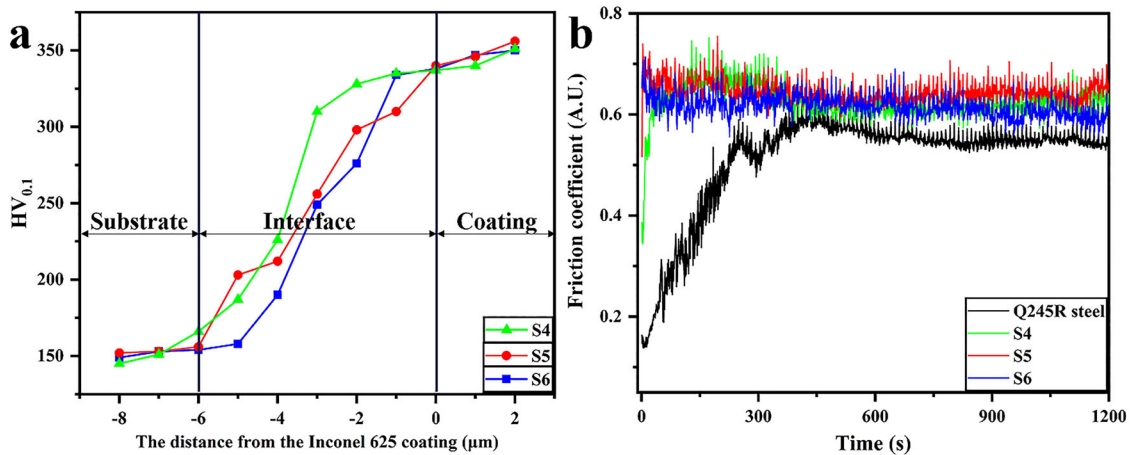


Fig. 6 An examination of the hardness and wear resistance of specimens. **a** Cross-section hardness of Inconel 625 coatings on Q245R steel: (S4, green), (S5, red), (S6, blue), respectively; **b** the friction coefficient curves of substrate: Q245R steel (black), and Inconel 625 coatings on Q245R steel: (S4, green), (S5, red), (S6, blue), respectively.

Table 2. Multiple variations in processing parameters of Inconel 625 coatings.

Number of specimens	Laser power (W)	Powder feeding rate (g/min)	Cladding speed (m/min)	Thickness of coating (μm)	Mass fraction of Fe element	Dilution rate
S1	1400	18.7	3	540	1.14	0.43
S2	1400	20.4	4	486	1.31	0.62
S3	1400	22.1	5	416	1.03	0.30
S4	1520	18.7	4	472	2.43	1.86
S5	1520	20.4	5	421	2.11	1.51
S6	1520	22.1	3	715	1.01	0.28
S7	1600	18.7	5	437	3.09	2.60
S8	1600	20.4	3	736	1.32	0.63
S9	1600	22.1	4	561	1.12	0.40

Table 3. Wear mass loss and bulk loss of Q245R, Inconel 625 coatings on Q245R steel (S4, S5, S6) after 1200 s friction and wear test.

Specimens	Density (g/cm ³)	Mass loss (g)	Bulk loss (cm ³)
Q245R steel	7.85	0.0043	5.48×10^{-4}
S4	8.4	0.0036	4.23×10^{-4}
S5	8.4	0.0033	3.93×10^{-4}
S6	8.4	0.0028	3.33×10^{-4}

coating and the substrate. As mentioned before, the top zone of coating (Fig. 2) is directly exposed to the air and the cooling rate of the top zone is larger than in other zones, fine equiaxed dendrites are formed at this zone, which results in the enhancement of microhardness.

Friction and wear tests were carried out on the Q245R steel substrate and Inconel 625 coatings surface, as shown in Fig. 6b. With the change of time, the friction coefficient also jittered up and down, and the friction coefficient of the cladding layer was different at a different dilution rate (S4, S5, and S6). The Q245R steel substrate exhibits a minimum friction coefficient and a maximal bulk worn loss after 1200 s abrasion treatment. The friction coefficient of Q245R steel substrate increases rapidly at the beginning, then tends to be stable. Compared to the Q245R steel substrate, the Inconel 625 coatings exhibit a larger friction coefficient and a smaller bulk worn loss. From Table 3, it can be found that the mass loss decreases with the decrease of dilution rate, indicating the wear resistance increases with the decrease of dilution rate. The reason for this phenomenon is that a few additional elements in the substrate were introduced into the cladding layer. During the high-speed laser cladding process, the feeding powders were melted by a high-intensity laser beam before injecting into the molten pool of substrate generating strong metallurgical bonding between cladding layers and substrate, and reducing the heat input to the substrate as well. In addition, dynamic recrystallization (involving dislocation tangles, and sub-grains) during the high-speed laser cladding process also can enhance the wear resistance of Inconel 625 coatings^{38,39}.

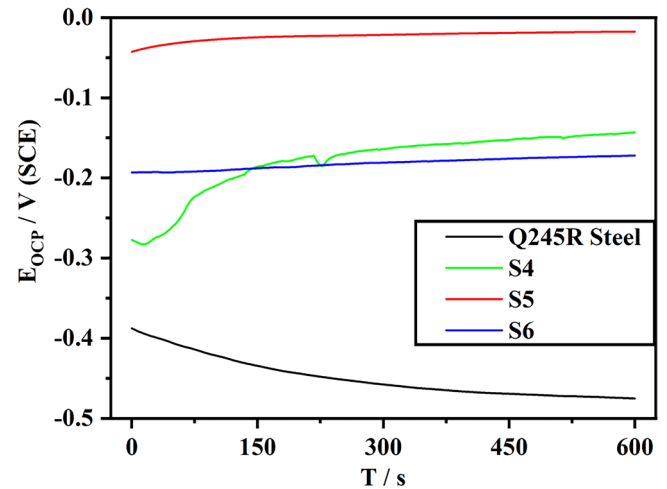
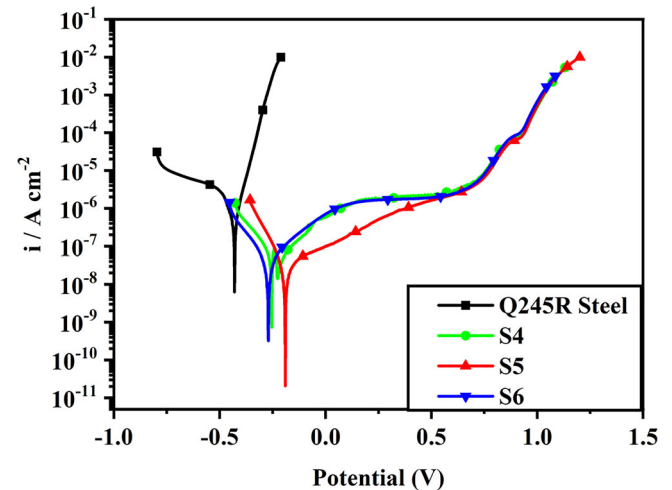
Corrosion properties

The corrosion resistance of Q245R steel substrate and Inconel 625 coatings were tested by an electrochemical method based on the three electrodes system. As shown in Fig. 7, the open-circuit-potential curve of Q245R steel substrate and Inconel 625 coatings were given. Plots from open-circuit potential measurement showed the Q245R steel exhibited the highest thermodynamic tendency to corrode with -0.4751 V open-circuit-potential. The open-circuit potentials of the Inconel 625 coated specimens were displaced in a positive direction, i.e., were higher than that of the Q245R steel substrate specimens. For the Inconel 625 coatings, the values are -0.1433 V for S4, -0.0174 V for S5, and -0.1721 V for S6, respectively (Table 4). Consequently, a great improvement in the thermodynamic tendency to corrode is achieved by the preparation of the Inconel 625 coatings on the surface of Q245R steel.

As shown in Fig. 8, the polarization curve of Q245R steel substrate and Inconel 625 coatings were given to evaluate their corrosion resistance. For the Q245R steel substrate, the corresponding self-corrosion potential is 0.4303 V, and the corresponding self-corrosion current density is 5.414×10^{-7} A/cm². For the Inconel 625 coatings, the values are -0.2546 V and 4.008×10^{-8} A/cm² for S4, -0.1905 V and 1.121×10^{-8} A/cm² for S5, and -0.2704 V and 1.1801×10^{-8} A/cm² for S6, respectively (Table 5). It is obvious that all Inconel 625 coatings possess a higher self-corrosion potential and a lower self-corrosion current density,

Table 4. The corresponding open-circuit-potential of Q245R steel substrate and Inconel 625 coatings: S4, S5, S6.

Samples	EOCP (V vs. SCE)
Q245R steel substrate	-0.4751
S4	-0.1433
S5	-0.0174
S6	-0.1721

**Fig. 7** The open-circuit-potential curve of Q245R steel substrate (black) and Inconel 625 coatings on Q245R steel: S4 (green), S5 (red), S6 (blue).**Fig. 8** The polarization curve of Q245R steel substrate (black) and Inconel 625 coatings on Q245R steel: S4 (green), S5 (red), S6 (blue).

suggesting that the Inconel 625 coatings have better corrosion resistance under the experimental conditions. In addition, the cathodic Tafel slope (β_c) and anodic Tafel slope (β_a) were also given in Table 5. The slope of the cathode (β_c) section of the potentiodynamic polarization curve for the Inconel 625 coated specimen is lower compared to the Q245R steel substrate (Table 5), and the β_c for Inconel 625 coatings: S4, S5 and S6 are similar. Moreover, the anode segment slope (β_a) of the linear sweep voltammetry curves for the Inconel 625 coated specimen is higher than the Q245R steel substrate (Table 5). From the polarization curves of S4, S5, and S6, it can be found that the proper dilution

Table 5. The corresponding self-corrosion potential, corresponding self-corrosion current density, β_a , and β_c , of Q245R steel substrate and Inconel 625 coatings: S4, S5, S6.

Samples	E_{corr} (V vs SCE)	j_{corr} (A/cm ²)	β_a (mV/dec)	β_c (mV/dec)
Q245R steel substrate	-0.4303	5.414×10^{-7}	38.428	83.464
S4	-0.2546	4.008×10^{-8}	46.201	45.547
S5	-0.1905	1.121×10^{-8}	70.286	48.851
S6	-0.2704	1.1801×10^{-8}	49.428	48.346

Table 6. Polarization resistance (R_p) and corrosion rate (CR) of Q245R steel substrate and Inconel 625 coatings: S4, S5, S6.

Samples	R_p (m Ω /cm ²)	CR (mm/year)
Q245R steel substrate	21.10	0.628
S4	248.48	0.223
S5	1116.34	0.062
S6	899.29	0.066

rate benefit improves the corrosion resistance of Inconel 625 coating, and the dynamics tendency to corrode: S5 > S4 > S6 > Q245R steel. Since some additional elements in the substrate were introduced into the Inconel 625 coatings, the formation of a corrosion-resistant phase in the coating. Therefore, controlling the dilution rate of the cladding layer is a prerequisite for obtaining an excellent corrosion-resistant Inconel 625 coating.

The value of the polarization resistance (R_p) of the Q245R steel substrate, and Inconel 625 coatings: S4, S5, and S6 in an aggressive chloride environment were collected in Table 6. The polarization resistance (R_p) of the electrode (Q245R steel substrate, and Inconel 625 coatings: S4, S5, and S6) is described by the Eq. (3)^{40–43}:

$$R_p = \frac{\beta_c \beta_a}{2.303 j_{\text{corr}} (\beta_a + \beta_c)} \quad (3)$$

The results suggest that all specimen surface covered with Inconel 625 coatings has higher polarization resistance of the electrode than that of Q245R steel substrate. The significant increase in the R_p value for Inconel 625 coated specimen was attributed to probably nickel and chromium oxides⁴⁰. Therefore, during the electrode process, the mass and charge exchange between the electrode and the electrolyte solution slows down.

The corrosion rate (CR) of the Q245R steel substrate, and Inconel 625 coatings: S4, S5, and S6 were calculated in Table 6 based on

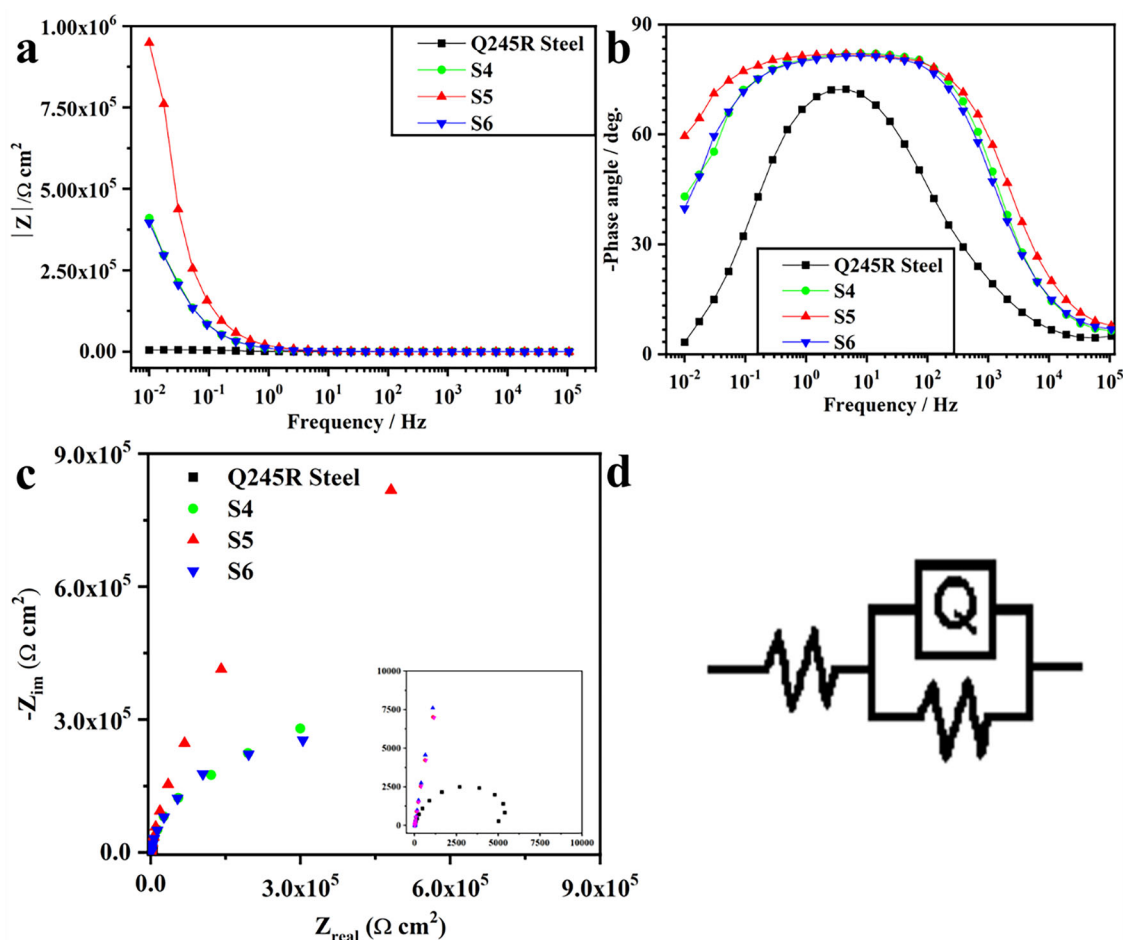


Fig. 9 The electrochemical impedance spectroscopy of Q245R steel substrate (black) and Inconel 625 coatings on Q245R steel: S4 (green), S5 (red), S6 (blue). **a** Bode plots (frequency); **b** bode plots (phase angle); **c** nyquist plots; **d** equivalent electrical circuit curve according to (a).

the Eq. (4), which is recommended by ASTM G102-89 (2004)⁴⁴:

$$CR = K_1 \frac{j_{\text{corr}}}{\rho} EW \quad (4)$$

where $j_{\text{corr}} = \mu\text{A}/\text{cm}^2$, $k_1 = 3.27 \times 10^{-3} \text{ mm g } \mu\text{A}^{-1} \text{ cm}^{-1} \text{ year}^{-1}$, $\rho = 7.8 \text{ g}/\text{cm}^3$ (Q245R steel), $\rho = 8.4 \text{ g}/\text{cm}^3$ (Inconel 625 coatings); equivalent weight, $EW = 27.93$ (Q245R steel), $EW = 24.82$ (Inconel 625 coatings).

The surface corrosion rate of Q245R steel substrate is high, the value of the corrosion rate was 0.628 mm/year. A drastic reduction in the corrosion rate of the tested specimen surface covered with Inconel 625 coatings. The results turned out that the CR of the Inconel 625 coating (S6) is over ten times lower compared to that of the Q245R steel substrate in an aggressive chloride environment (Table 6).

To further verify the above conclusions, the electrochemical impedance spectroscopy (EIS) and equivalent electric circuit curve are given in Fig. 9. From bode plots (Fig. 9a), the impedance of the Inconel 625 coated specimens is bigger than that of Q245R steel substrate at low frequencies (0.01 Hz). It means that a great improvement in the dynamics tendency to corrode is achieved by the preparation of the Inconel 625 coatings on the surface of Q245R steel substrate⁴⁰. In addition, the results show that the impedance value of Inconel 625 coated specimens is independent

of its dilution rate, and a high dilution rate have a negative impact on its impedance value. From the EIS curves of S4, S5, and S6, it can be found that when the dilution rate is 1.51 (S5), the impedance reaches the maximum. This phenomenon is caused by increasing additional elements in the substrate introduced into the Inconel 625 coatings deterioration of its corrosion resistance. According to Bode-phase angle plots in Fig. 9b, more dispersed points were obtained in all frequency ranges for Inconel 625 coated specimens. It means that a great improvement in the dynamics tendency to corrode is achieved by the preparation of the Inconel 625 coatings on the surface of the Q245R steel substrate. It means that Inconel 625 coated specimens possess better corrosion resistance than Q245R steel substrate^{40,42}. Nyquist plots in Fig. 9c show that low real and imaginary impedance values for Q245R steel substrate exposed to NaCl solution (3.5 wt%) are attributed to the chemical composition of the water cut extracted^{45,46}. Compared with the Q245R steel substrate, all Inconel 625 coated specimens exhibit better corrosion resistance tendency, due to their bigger real and imaginary impedance values. Among the capacitive and charge transfer resistance elements (CPE and R_{ct} values listed in Table 7), it is evident that impedance spectra of Q245R steel substrate increased with Inconel 625 coated. The equivalent electrical circuit curve shown in Fig. 9d is used to model the EIS spectra (Fig. 9c). Electronic elements in Fig. 9d have the following meanings: R_s is the electrolyte resistance between the working and reference electrode; R_p is the polarization resistance and is inversely proportional to the corrosion current density; Q is the constant phase angle element (CPE) used to replace the interfacial capacitance, where Y_0 is a constant which may depend on the electrode potential, and n is the frequency power: the capacitive characteristic is more obvious if n is large, otherwise the resistive property is more obvious when the n is small. R_{ct} is the resistance of materials. These results further confirmed that the lower CEP and higher R_{ct} will lead to better corrosion resistance for Inconel

Samples	R_s (ohm cm^2)	CPE, Y_0 (sec^n/cm^2)	n ($0 < n < 1$)	R_{ct} (ohm cm^2)
Q245R steel substrate	12.11	2.037×10^{-4}	0.8111	6271
S4	9.923	1.866×10^{-5}	0.9106	5.686×10^5
S5	13.08	1.025×10^{-5}	0.9066	4.004×10^6
S6	11.23	1.895×10^{-5}	0.9033	5.638×10^5

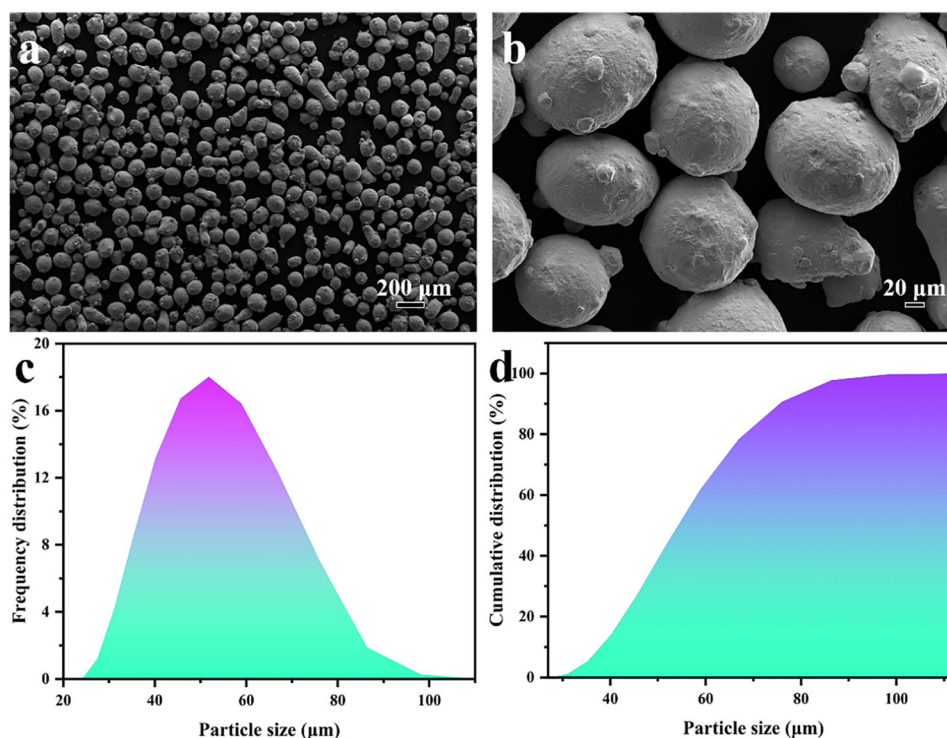


Fig. 10 Microstructure and particle size distribution of Inconel 625 powder. **a** FESEM image; **b** locally magnified FESEM image of the **a**; **c**, **d** particle size distribution.

625 coated specimens than Q245R steel substrate, as shown in Table 7, and the corrosion resistance: S5 > S4 > S6 > Q245R steel.

In this work, the phase composition, microstructure evolution, microhardness, wear, and corrosion resistance behavior of high-speed laser cladding Inconel 625 coating are analyzed. The main conclusion can be drawn as follows:

- (1) The Inconel 625 coating was mainly composed of the γ -Ni phase and the Nb/Mo-enriched laves phase. Cellular crystal, columnar crystal, and equiaxed dendrites appear in the bottom, middle, and top of the Inconel 625 coatings, respectively.
- (2) The average microhardness of Inconel 625 coatings was recorded as 350 HV_{0.1}, which is ~2.3 times higher than that of Q245R steel substrate. The size relationship of the hardness in the top of the coating, the hardness in the middle of the coating, the hardness in the bottom of the coating, and the hardness of the Q245R steel substrate is as follows: the hardness in the top of coating > the hardness in the middle of coating > the hardness in the bottom of coating > the hardness of the Q245R steel substrate. The differences between the hardness in the top of the coating, the hardness in the middle of the coating, and the hardness in the bottom can be ascribed to the significant difference in microstructure in the different parts of the coating.
- (3) The wear and corrosion resistance of the Inconel 625 coatings was better than the Q245R steel substrate.

METHODS

Materials preparation

Figure 10 shows the size, shape, and distribution of Inconel 625 powder. Commercial-grade Inconel 625 powder (Höganäs, Sweden) with a nominal size range of 24.1–98.1 μm was used to perform the subsequent high-speed laser cladding process. The chemical composition of Inconel 625 powder was analyzed by an inductively coupled plasma optical emission spectrometer (ICPE-9800, Shimadzu, Japan) and the results are given in Table 8. The square-shaped Q245R structure steel with a length of 100 mm, a width of 100 mm, and a thickness of 5 mm were used as the substrate.

Table 8. Chemical composition of Inconel 625 powder (wt.%).

Ni	Cr	Mo	Cu	Sd	Sn	Nb	Fe	Co	Mn
63.35	21.87	9.5	0.324	0.023	0.05	3.64	0.753	0.066	0.39

Prior to high-speed laser cladding, the Inconel 625 powders were dried in the oven for 1 h at 120 °C. Meanwhile, each substrate was ground using 400-grit SiC sandpaper, and then was ultrasonically cleaned by utilizing deionized water and ethanol three times.

Coating deposition

High-speed laser cladding Inconel 625 coatings were fabricated by utilizing fiber laser (ZKZM-4000, ZKZM, China) operated in continuous mode with maximum laser power of 4000 W. The powder was injected into a laser molten pool with coaxial powder feeding driven by argon at a flow rate of 1.5 L/min. Figure 11 shows a schematic illustration of the high-speed laser cladding process. As shown in Fig. 11, the experiment was carried out in a protective chamber where the steam of argon as shielding gas was continually supplied at a flow rate of 14.5 L/min to prevent oxidation of the molten metal region. The overlapping of all Inconel 625 coatings specimens is 80%.

To ensure better wear and corrosion resistance, proper process parameters must be adopted, such as laser power, powder feeding rate, and cladding speed, which have a significant influence on the thickness of the Inconel 625 coatings layer, microstructural uniformity, dilution rate, and mechanical properties. Here, multiple variations in laser power, powder feeding rate, and cladding speed were carried out to obtain the optimal processing parameters, as shown in Table 9.

Characterizations

The X-ray diffraction patterns of Q245R steel substrate and Inconel 625 coatings, Inconel 625 powder at different temperatures were collected by using an X-ray diffraction station in Beijing Synchrotron Radiation Facility (BSRF) with wavelength = 0.15401 nm. The scans were recorded between 20° and 120° with a step size of 0.02°. The microstructures of high-speed laser-clad specimens were characterized by secondary electron and electron backscattered diffraction (EBSD) techniques in a field emission gun scanning electron microscope (FESEM, ZEISS SUPRA55). The collected EBSD data was processed with Channel 5 analysis software. The microstructures and phase structure were analyzed by means of transmission electron microscopy (TEM, TecnaiG2F30 field emission transmission electron microscope).

The three-dimensional (3D) surface morphology of the Inconel 625 coating specimen (S6) was characterized by a white-light interferometer (State Key Laboratory of Tribology, Tsinghua University). The optical interference method was used for quantitative measurement of the 3D surface texture images, microscopic linear height, and average surface roughness (Ra) of the Inconel 625 coating specimen.

The microhardness of coated specimens was performed using a Vickers microhardness tester (Nano Indenter II) to measure the cross-sectional hardness of the coatings. The selected test load was 0.3 kg and dwell time was set to 15 s. The vertical profile from cladded region to the Q245R steel substrate was acquired. A minimum of three adjacent indents were performed and the average value was recorded. The linear friction and

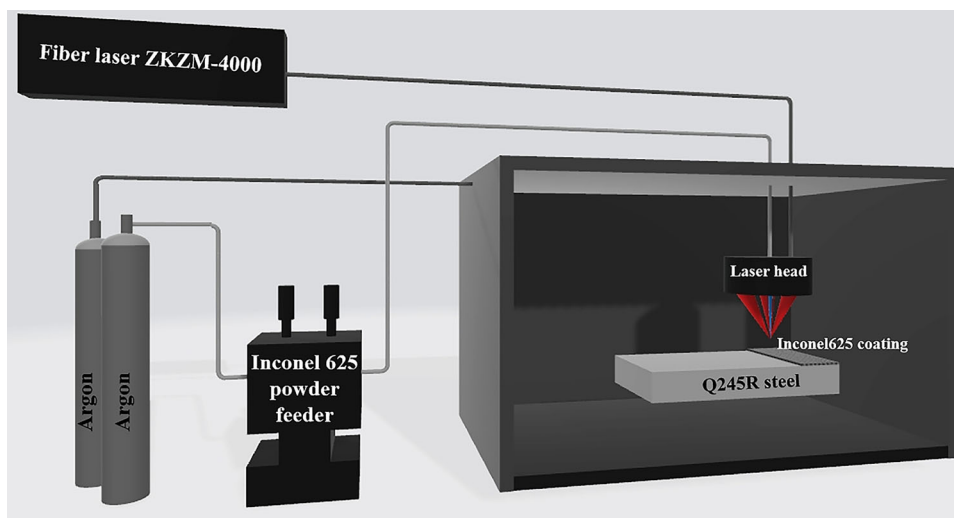


Fig. 11 Schematic diagrams of Inconel 625 superalloy deposited on the Q245R structure steel by high-speed laser cladding.

Table 9. Multiple variations in processing parameters of Inconel 625 coatings.

Number of specimens	Laser power (W)	Powder feeding rate (g/min)	Cladding speed (m/min)
S1	1400	18.7	3
S2	1400	20.4	4
S3	1400	22.1	5
S4	1520	18.7	4
S5	1520	20.4	5
S6	1520	22.1	3
S7	1600	18.7	5
S8	1600	20.4	3
S9	1600	22.1	4

wear test of the Q245R steel substrate and Inconel 625 coatings specimens in the length direction were carried out by using a Rtec MFT-5000 friction and wear instrument. The reciprocating sliding mode was used in the experiment. The coupling parts were Si₃N₄ ceramic balls with a load of 30 N, a single sliding length of 30 mm, a sliding speed of 5 mm/s, and a sliding time of 20 min.

The corrosion resistance of Q245R steel substrate and Inconel 625 coatings were tested by an electrochemical method based on a three electrodes system (the three-electrode system electrolytic cell with Pt sheet as counter electrode and Ag/AgCl electrode as reference electrode). All the specimens were encapsulated by rosin in the PVC tube with a size of 30 mm. Only one side of the specimens were exposed to the outside during the encapsulating process. The NaCl solution with a mass fraction of 3.5% was selected as the electrolyte. Before the electrochemical test, the Q245R steel substrate and Inconel 625 coatings samples were soaked in the electrolyte until the stable open-circuit potentials were reached. The electrochemical impedance spectra (EIS) were measured in the scope of 10⁵–0.01 Hz with the applied AC perturbation amplitude of 5 mV. The ZSimpWin (Version 3.5) software was used to analyzed the EIS data. The potentiodynamic polarization curves of Q245R steel substrate and Inconel 625 coatings samples were measured in the scope of –0.5 to 1.0 V (vs RHE) using the scan rate of 0.5 mV/s.

DATA AVAILABILITY

The data that support the findings of this study are available from the corresponding author upon reasonable request.

Received: 17 November 2021; Accepted: 5 April 2022;

Published online: 25 April 2022

REFERENCES

- Liu, Z. D. et al. High temperature corrosion behaviors of 20G steel, hastelloy C22 alloy and C22 laser coating under reducing atmosphere with H₂S. *Coatings* **10**, 617 (2020).
- Yang, W. et al. Effects of near-wall air application in a pulverized-coal 300 MWe utility boiler on combustion and corrosive gases. *Energ. Fuel* **31**, 10075 (2017).
- Pardo, A. et al. Pitting corrosion behaviour of austenitic stainless steels—Combining effects of Mn and Mo additions. *Corros. Sci.* **50**, 1796 (2008).
- Liu, S. et al. A comparative study on the high temperature corrosion of TP347H stainless steel, C22 alloy and laser-cladding C22 coating in molten chloride salts. *Corros. Sci.* **83**, 396 (2014).
- Zhang, Z., Yu, T. & Kovacevic, R. Erosion and corrosion resistance of laser cladded AISI 420 stainless steel reinforced with VC. *Appl. Surf. Sci.* **410**, 225 (2017).
- Gui, W. Y. et al. Cathode electrolytic plasma deposition of (Al_{0.9}Cr_{0.1})₂O₃/γ-Al₂O₃ composite coatings onto Ti45Al8.5Nb0.1Y0.2W alloys for high-temperature applications. *Materialia* **15**, 101002 (2021).
- Galedari, S. A. et al. A comprehensive review of corrosion resistance of thermally-sprayed and thermally-diffused protective coatings on steel structures. *J. Therm. Spray. Techn.* **28**, 645 (2019).
- Arora, H. S. et al. Facile and green engineering approach for enhanced corrosion resistance of Ni-Cr-Al₂O₃ thermal spray coatings. *ACS Omega* **5**, 24558 (2020).
- Alidokht, S. A. et al. Cold spray deposition of Ni and WC-reinforced Ni matrix composite coatings. *J. Therm. Spray. Techn.* **26**, 1908 (2017).
- Shi, Z. P. et al. Effect of Ni interlayer on cavitation erosion resistance of NiTi cladding by tungsten inert gas (TIG) surfacing process. *Acta Metall. Sin.* **33**, 91 (2020).
- Li, X. et al. Manufacturing of Ti₃SiC₂ lubricated Co-based alloy coatings using laser cladding technology. *Opt. Laser Technol.* **114**, 209 (2019).
- Yuan, W. Y. et al. A comparative study on microstructure and properties of traditional laser cladding and high-speed laser cladding of Ni45 alloy coatings. *Surf. Coat. Technol.* **405**, 126582 (2021).
- Kattire, P. et al. Experimental characterization of laser cladding of CPM 9Von H13 tool steel for die repair applications. *J. Manuf. Process.* **20**, 492 (2015).
- Lou, L. et al. High speed laser cladded Ti-Cu-NiCoCrAlTaY burn resistant coating and its oxidation behavior. *Surf. Coat. Technol.* **392**, 125697 (2020).
- Weng, F., Chen, C. Z. & Yu, H. J. Research status of laser cladding on titanium and its alloys: a review. *Mater. Des.* **58**, 412 (2014).
- Zhu, L. D. et al. Recent research and development status of laser cladding: a review. *Opt. Laser Technol.* **138**, 106915 (2021).
- Shen, F. M. et al. Effect of microstructure on the corrosion resistance of coatings by extreme high speed laser cladding. *Appl. Surf. Sci.* **517**, 146085 (2020).
- Chen, L. & Bai, S. L. The anti-corrosion behavior under multi-factor impingement of Hastelloy C22 coating prepared by multilayer laser cladding. *Appl. Surf. Sci.* **437**, 1 (2018).
- Hu, Y. L. et al. Effect of solution heat treatment on the microstructure and mechanical properties of Inconel 625 superalloy fabricated by laser solid forming. *J. Alloy. Compd.* **767**, 330 (2018).
- Schopphoven, T. et al. Investigation on ultra-high-speed laser material deposition as alternative for hard chrome plating and thermal spraying. *J. Laser Appl.* **28**, 002501 (2016).
- Schopphoven, T., Gasser, A. & Backes, G. EHLA: extreme high-speed laser material deposition—economical and effective protection against corrosion and wear. *Laser Tech. J.* **4**, 26 (2017).
- Li, S. et al. Microstructure characteristics of Inconel 625 superalloy manufactured by selective laser melting. *J. Mater. Sci. Technol.* **31**, 946 (2015).
- Carroll, B. E. et al. Functionally graded material of 304L stainless steel and Inconel 625 fabricated by directed energy deposition: characterization and thermo-dynamic modeling. *Acta Mater.* **108**, 46 (2016).
- Mostafaei, A. et al. Microstructural evolution and mechanical properties of differently heat-treated binder jet printed samples from gas- and water-atomized alloy 625 powders. *Acta Mater.* **124**, 280 (2017).
- Chaudhuri, A. et al. Microstructural evolution of cold-sprayed Inconel 625 superalloy coatings on low alloy steel substrate. *Acta Mater.* **129**, 11 (2017).
- Lass, E. A. et al. Precipitation and dissolution of δ and γ' during heat treatment of a laser powder-bed fusion produced Ni-based superalloy. *Scr. Mater.* **154**, 83 (2018).
- Feng, K. et al. Improved high-temperature hardness and wear resistance of Inconel 625 coatings fabricated by laser cladding. *J. Mater. Process. Tech.* **243**, 82 (2017).
- Kou, S. *Welding Metallurgy* 2nd ed. (John Wiley & Sons, Inc., 2003).
- Oliveira, J. P., LaLonde, A. D. & Ma, J. Processing parameters in laser powder bed fusion metal additive manufacturing. *Mater. Des.* **193**, 108762 (2020).
- Basak, A., Acharya, R. & Das, S. Additive manufacturing of single-crystal superalloy CMSX-4 through scanning laser epitaxy: computational modeling, experimental process development, and process parameter optimization. *Metall. Mater. Trans. A* **47**, 3845 (2016).
- Wang, L. & Wang, N. Effect of substrate orientation on the formation of equiaxed stray grains in laser surface remelted single crystal superalloys: experimental investigation. *Acta Mater.* **104**, 250 (2016).
- Kreitzberg, A., Brailovski, V. & Turenne, S. Effect of heat treatment and hot isostatic pressing on the microstructure and mechanical properties of Inconel 625 alloy processed by laser powder bed fusion. *Mater. Sci. Eng. A-Struct.* **689**, 1 (2017).
- AlMangour, B., Grzesiak, D. & Yang, J. M. Rapid fabrication of bulk-form TiB₂/316L stainless steel nanocomposites with novel reinforcement architecture and improved performance by selective laser melting. *J. Alloy. Compd.* **680**, 480 (2016).
- Kannan, T. & Yonganandh, J. Effect of process parameters on clad bead geometry and its shape relationships of stainless steel claddings deposited by GMAW. *Int. J. Adv. Manuf. Tech.* **47**, 9 (2010).
- Xi, W. C. et al. Geometry and dilution rate analysis and prediction of laser cladding. *Int. J. Adv. Manuf. Tech.* **103**, 4695 (2019).
- Song, B., Voisey, K. T. & Hussain, T. High temperature chlorine-induced corrosion of Ni50Cr coating: HVOLF, HVOGF, cold spray and laser cladding. *Surf. Coat. Technol.* **337**, 357 (2018).

37. Yu, T. B. et al. Experimental research and multi-response multi-parameter optimization of laser cladding Fe313. *Opt. Laser Technol.* **108**, 321 (2018).
38. Huang, R. R. et al. Dynamic recrystallization-induced temperature insensitivity of yield stress in single-crystal Al_{1.2}CrFeCoNi micropillars. *Sci. China Technol. Sc.* **64**, 11 (2021).
39. Chen, J. Y. et al. Deformation mechanisms in a fine-grained Udimet 720LI nickel-base superalloy with high volume fractions of γ' phases. *Mater. Sci. Eng. A-Struct.* **673**, 122 (2016).
40. Sende, M., Staszewska-Samson, K. & Danielewski, H. Corrosion behavior of Inconel 625 coating produced by laser cladding. *Coatings* **11**, 759 (2021).
41. Jiang, J., Yu, L. & Gan, F. High temperature naphthenic acid corrosion of steel in high TAN refining media. *Anti-Corros. Methods Mater.* **55**, 257 (2008).
42. Quej Ake, L. M., Contreras, A. & Aburto, J. The effect of non-ionic surfactant on the internal corrosion for X52 steel in extra-heavy crude oil-in-water emulsions. *Anti-Corros. Methods Mater.* **65**, 234 (2018).
43. Yang, G. et al. Corrosion behavior of 20# steel in aqueous CO₂ solution under stratified gas-liquid two-phase flow condition. *Anti-Corros. Methods Mater.* **66**, 11 (2019).
44. ASTM G102-89. *Standard Practice for Calculation of Corrosion Rates and Related Information from Electrochemical Measurements* (ASTM, 2004).
45. Cheng, Q. et al. Corrosion behaviour of Q235B carbon steel in sediment water from crude oil. *Corros. Sci.* **111**, 61 (2016).
46. Zhu, S. D. et al. Corrosion of N80 carbon steel in oil field formation water containing CO₂ in the absence and presence of acetic acid. *Corros. Sci.* **53**, 3156 (2011).

ACKNOWLEDGEMENTS

The authors appreciate the financial support from the Fundamental Research Funds for the Central Universities (NO. FRF-TP-19-080A1); China Postdoctoral Science Foundation (No. 2019M660452); State Key Lab of Advanced Metals and Materials (No. 2020-Z07 and 2021-ZD01); National Natural Science Foundation of China (No. 52101070 and No. 51831001); Jiangxi Provincial Natural Science Foundation (No. 20212BAB214052) and Creative Research Groups of China (No. 51921001). Thanks eceshi (www.eceshi.com) for the electrochemical analysis.

AUTHOR CONTRIBUTIONS

The idea was proposed by W.G. The experiments were carried out by W.G., C.Z., and J.G. The experimental results were analyzed and interpreted by W.G., Y.D., X.W., Y.L., and Y.Q. W.G. wrote the main manuscript, and the manuscript was reviewed by Y.Q., J.Q., and J.L.

COMPETING INTERESTS

The authors declare no competing interests.

ADDITIONAL INFORMATION

Correspondence and requests for materials should be addressed to Yuhai Qu or Junpin Lin.

Reprints and permission information is available at <http://www.nature.com/reprints>

Publisher's note Springer Nature remains neutral with regard to jurisdictional claims in published maps and institutional affiliations.



Open Access This article is licensed under a Creative Commons Attribution 4.0 International License, which permits use, sharing, adaptation, distribution and reproduction in any medium or format, as long as you give appropriate credit to the original author(s) and the source, provide a link to the Creative Commons license, and indicate if changes were made. The images or other third party material in this article are included in the article's Creative Commons license, unless indicated otherwise in a credit line to the material. If material is not included in the article's Creative Commons license and your intended use is not permitted by statutory regulation or exceeds the permitted use, you will need to obtain permission directly from the copyright holder. To view a copy of this license, visit <http://creativecommons.org/licenses/by/4.0/>.

© The Author(s) 2022